


Article

VOCs Photothermo-Catalytic Removal on $\text{MnO}_x\text{-ZrO}_2$ Catalysts

Roberto Fiorenza ^{*}, Roberta Agata Farina, Enrica Maria Malannata, Francesca Lo Presti and Stefano Andrea Balsamo

Dipartimento di Scienze Chimiche, Università di Catania, Viale A. Doria 6, 95125 Catania, Italy; roberta.agata.farina@gmail.com (R.A.F.); enrica.malannata@phd.unict.it (E.M.M.); francesca.lopresti@phd.unict.it (F.L.P.); stefano.balsamo@phd.unict.it (S.A.B.)

* Correspondence: rfiorenza@unict.it; Tel.: +39-0957385012

Abstract: Solar photothermo-catalysis is a fascinating multi-catalytic approach for volatile organic compounds (VOCs) removal. In this work, we have explored the performance and the chemico-physical features of non-critical, noble, metal-free $\text{MnO}_x\text{-ZrO}_2$ mixed oxides. The structural, morphological, and optical characterizations of these materials pointed to as a low amount of ZrO_2 favoured a good interaction and the ionic exchange between the Mn and the Zr ions. This favoured the redox properties of MnO_x increasing the mobility of its oxygens that can participate in the VOCs oxidation through a Mars-van Krevelen mechanism. The further application of solar irradiation sped up the oxidation reactions promoting the VOCs total oxidation to CO_2 . The $\text{MnO}_x\text{-5 wt.\%ZrO}_2$ sample showed, in the photothermo-catalytic tests, a toluene T_{90} (temperature of 90% of conversion) of 180 °C and an ethanol T_{90} conversion to CO_2 of 156 °C, 36 °C, and 205 °C lower compared to the thermocatalytic tests, respectively. Finally, the same sample exhibited 84% toluene conversion and the best selectivity to CO_2 in the ethanol removal after 5 h of solar irradiation at room temperature, a photoactivity similar to the most employed TiO_2 -based materials. The as-synthesized mixed oxide is promising for an improved sustainability in both catalyst design and environmental applications.



Citation: Fiorenza, R.; Farina, R.A.; Malannata, E.M.; Lo Presti, F.; Balsamo, S.A. VOCs Photothermo-Catalytic Removal on $\text{MnO}_x\text{-ZrO}_2$ Catalysts. *Catalysts* **2022**, *12*, 85. <https://doi.org/10.3390/catal12010085>

Academic Editor: Xintong Zhang

Received: 27 December 2021

Accepted: 12 January 2022

Published: 13 January 2022

Publisher's Note: MDPI stays neutral with regard to jurisdictional claims in published maps and institutional affiliations.



Copyright: © 2022 by the authors. Licensee MDPI, Basel, Switzerland. This article is an open access article distributed under the terms and conditions of the Creative Commons Attribution (CC BY) license (<https://creativecommons.org/licenses/by/4.0/>).

Keywords: VOC; photothermo catalysis; toluene; ethanol; manganese oxide; zirconium oxide

1. Introduction

Nowadays, the quality of air, both in indoor and outdoor environments, is an extremely important concern. Furthermore, the COVID-19 emergency has pointed to the necessity of clean air to discourage virus infection. Among the air pollutants, volatile organic compounds (VOCs) include many of the most dangerous substances for both human health and the environment. Different strategies were employed to remove VOCs from the air, and an innovative and sustainable solution is represented by solar photocatalytic or photothermo-catalytic oxidation [1,2]. Compared to the most used catalytic or non-catalytic VOCs combustion, the photocatalytic process allows one to exploit solar irradiation with green advantages to work at milder conditions using renewable energy [2]. However, the performance of the photocatalysts is much lower compared to the catalysts employed for the thermocatalytic removal of VOCs [3], and for these reasons, the multi-catalytic approach of the photothermo-catalysis is a fascinating way to obtain high VOCs removal values of thermocatalysis but at lower temperatures, increasing, at the same time, the energy efficiency of the process. To design performing photothermo catalysts, different properties are required [4,5]. Analogously to photocatalysis, it is necessary to have a semiconductor material that, after solar irradiation, is able to generate photoelectrons and photoholes in its conduction (CB) and valence (VB) bands, respectively. It should have redox properties activated with the temperature; in this way, the superficial/mobile oxygens of the catalyst or of the support can participate in the oxidation of VOCs increasing the overall activity [3,6]. Finally, the photothermo catalysts should be resistant to both long-time irradiation and heating. The preparation of mixed oxides or composites is the

best and easiest way to combine all of these features. Indeed, with the formation of a suitable heterojunction, it is possible to exploit solar irradiation, decreasing the bandgap (E_g) of the main semiconductor oxide, profiting from both the photocatalytic activity of the principal oxides and the thermocatalytic activity of the hosted oxide. Moreover, the introduction of host ions in the lattice of the main oxide allows one to create defects and oxygen vacancies that favour VOCs oxidation [7,8].

The TiO₂-CeO₂ composites showed promising performance in the photo-thermal approach for both VOCs removal and CO₂ reduction [3,9]; however, one of the side effects of the current pandemic situation is the crisis of raw materials exportation, and as a consequence, in 2020, titanium featured in the EU critical raw materials list [10]. Considering that up until now, TiO₂ is the most studied and applied semiconductor, both in academia and in industrial research focused on photocatalytic applications, the exploration of unconventional non-critical (photo)catalysts is highly required.

In this work, we have investigated the photothermo-catalytic properties of MnO_x-ZrO₂ mixed oxides, with the aim of finding new and sustainable alternatives to the most common TiO₂-based photocatalysts, and without the addition of noble metal co-catalysts, usually used in the catalytic and photocatalytic removal of VOCs [11], to obtain even more environmentally friendly catalysts, in the end.

Manganese oxide exists in four stable forms (MnO, MnO₂, Mn₃O₄ and Mn₂O₃), and all of them own a semiconductor electronic structure characterized by the partially filled d orbitals which permit the electronic d-d transitions under UV or visible light irradiation [12]. Based on the preparation method, it is common to obtain a non-stoichiometric oxide or a mixture of different MnO_x oxides with the +II, +III and/or +IV oxidation states. The high mobility/reducibility of manganese oxide lattice oxygens is particularly useful for VOCs removal [13,14], whereas the redox properties of MnO_x can be particularly advantageous for the photothermo-catalytic oxidation of VOCs, as well as its low bandgap (in the range 2.0–3.5 eV depending of the crystalline structure [12,15]) that can allow a more efficient use of solar radiation.

Zirconium oxide (zirconia) was largely used as a support of several noble metal-based catalysts used for the thermocatalytic oxidation of VOCs, due to its high stability, thermal resistance, and ionic conductivity [16,17]. Furthermore, it is a large bandgap semiconductor (E_g of about 5.0 eV [18] or lower depending to the zirconia synthesis). Therefore, its coupling with a lower bandgap semiconductor (as MnO_x) can be a performing and fascinating strategy to reduce the odds of charge recombination (a common reason for photocatalysts deactivation) and to synergistically exploit both the thermal stability and the redox properties of MnO_x and ZrO₂ [19,20] together with their photocatalytic features.

We have also determined the chemico-physical and the photocatalytic, thermocatalytic and photothermo-catalytic activities of MnO_x-ZrO₂ oxides in the oxidation of toluene and ethanol, chosen as VOCs models, due to the high toxicity nature of toluene and to the wide use of ethanol as a solvent in many industrial processes and as an octane booster in combustion engines, whose incomplete oxidation can give the emission of dangerous compounds, as acetaldehyde, in the environment [21].

2. Results

2.1. Structural, Morphological, Textural and Optical Properties of the Samples

The XRD patterns of the analysed samples are shown in Figure 1. The precipitation of manganese chloride (II) with NaOH and the employed calcination temperature (600 °C for 2 h) allowed to obtain the Mn₃O₄. The signals at $2\theta = 18.1^\circ, 28.9^\circ, 31.0^\circ, 32.4^\circ, 36.0^\circ, 38.1^\circ, 44.3^\circ$ and 50.8° are, indeed, in accordance with the PDF card. No.: 00-080-0382 of pure Mn₃O₄ (Hausmannite). Bare ZrO₂ was obtained with the ammonia-driven precipitation of zirconyl nitrate. The signals fitted with the PDF card No. 00-079-1771 of zirconium oxide, with the typical diffraction peaks at $2\theta = 30.2^\circ, 35.2^\circ$ and 50.3° . Interestingly, the co-precipitation with NaOH of both metals salt precursors created substantial changes in the crystalline structure of manganese oxide. The addition of 5 wt.% of zirconium oxide

led to a mixed $\text{Mn}_2\text{O}_3/\text{Mn}_3\text{O}_4$ phase being present the diffraction peak at $2\theta = 32.9^\circ$; that is, the typical fingerprint of Mn_2O_3 (PDF card No. 00-071-0636, [12,22]), together with the signals at $2\theta = 38.2^\circ$ (overlapped with the signal of Mn_3O_4) and 55.1° that are also ascribed to manganese (III) oxide [12,22]. The increase of ZrO_2 content (MnO_x -10% ZrO_2 sample) restored the main presence of Mn_3O_4 with a trace of Mn_2O_3 . In both the mixed oxides, the signals related to ZrO_2 are absent, probably due to the low amount of hosted oxide and/or to the good dispersion of zirconium oxide on manganese oxide.

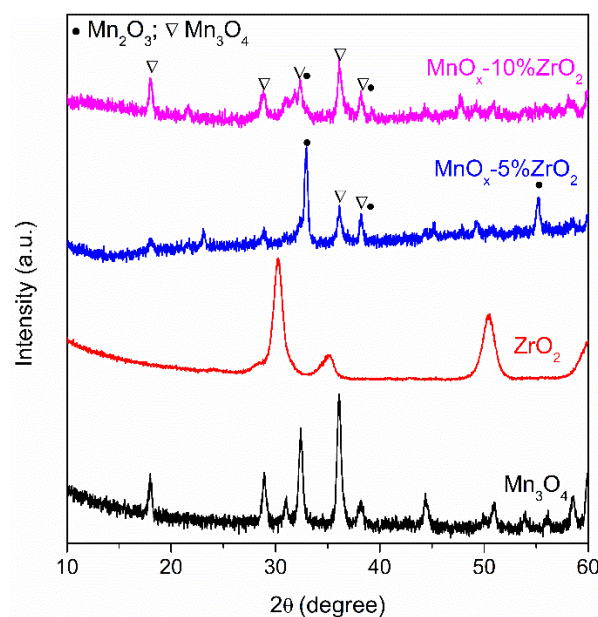


Figure 1. X-ray Diffraction (XRD) patterns of the examined samples.

The ion radius of Zr^{4+} (0.84 Å) is similar of Mn^{2+} (0.83 Å), and this can favour the ionic exchange between these cations [20,23]. On the contrary, the smaller radius of Mn^{3+} (0.64 Å) makes the $\text{Zr}^{4+}/\text{Mn}^{3+}$ exchange more difficult. Probably, when the amount of ZrO_2 is low, the Zr ions partially replace the Mn^{2+} promoting, in this way, the main presence of Mn^{3+} , whereas a higher amount of ZrO_2 led to a preferential surface covering of the MnO_x instead of a lattice incorporation of the zirconium ions in MnO_x [20,23]. Thus, it can explain the major presence of Mn (III) on MnO_x -5% ZrO_2 sample, and the coexistence of Mn II and III in the MnO_x -10% ZrO_2 . The main crystalline size of the samples (Table 1) was determined by applying the Scherrer formula on the principal diffraction peaks of the oxides ($2\theta = 36.0^\circ$ for Mn_3O_4 , 30.2° for ZrO_2 , 32.9° for MnO_x -5% ZrO_2 , whereas for MnO_x -10% ZrO_2 , the value was mediated considering both the $2\theta = 32.4^\circ$ and 36.0° signals). The addition of zirconium oxide led to a slight increase of the crystalline size of manganese oxide, whereas the bare ZrO_2 showed the lowest crystalline size (8 nm). However, this latter oxide, in accordance with the surface area values reported in the literature [18], showed the lowest surface area (Table 1, $26.2 \text{ m}^2/\text{g}$), whereas the bare Mn_3O_4 exhibited the highest BET surface area ($99.6 \text{ m}^2/\text{g}$). Compared to the bare Mn_3O_4 , the slight increase of the crystallite size of the mixed oxides determined a decrease of their surface area, which were about $85\text{--}86 \text{ m}^2/\text{g}$ for both the MnO_x - ZrO_2 samples (Table 1).

Table 1. Structural, textural and optical properties of the examined samples.

Sample	Crystallite Size (nm) ^a	BET Surface Area (m ² /g)	E _g (eV)
Mn ₃ O ₄	14.5	99.6	3.29
ZrO ₂	8.1	26.2	3.02
MnO _x -5%ZrO ₂	17.9	85.4	3.26
MnO _x -10%ZrO ₂	18.2	86.1	3.27

^a Estimated by XRD.

The SEM-EDX measurements (Figure 2) were performed to evaluate the presence of zirconium oxide on MnO_x. The adopted precipitation methods led to, indifferently to the investigated samples, a non-homogenous morphology with spherical particles (Figures 2a and S1). From the EDX elemental analysis (Figure 2b,c, Table 2), it is possible to note that a little surface segregation of zirconium in the MnO_x-10%ZrO₂ sample was detected, whose zirconium wt.% was 3.7 times higher (instead of twice as expected considering the nominal concentration) compared to the MnO_x-5%ZrO₂. In accordance with the XRD data, the increase of the amount of ZrO₂ led to an enrichment of zirconium oxide on the surface of MnO_x, whereas in the MnO_x-5%ZrO₂ mixed oxide, the ZrO₂ was mainly embedded in the lattice of MnO_x.

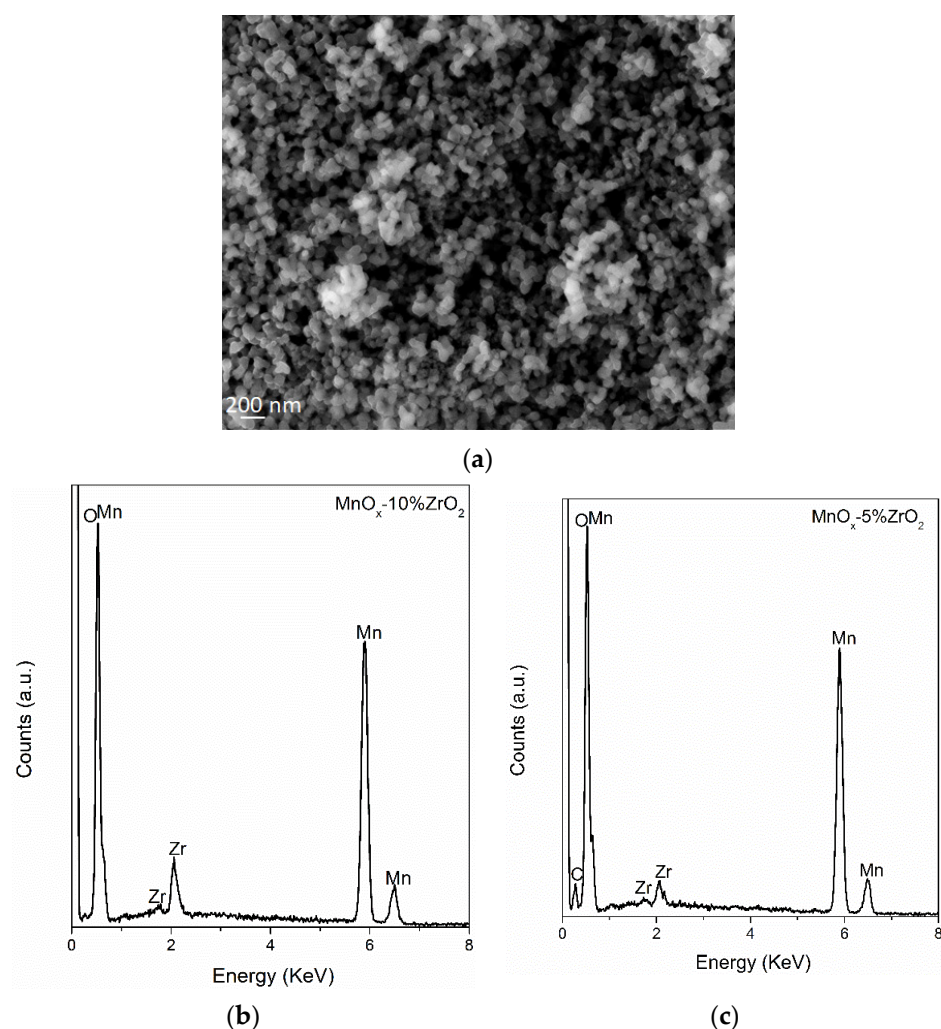


Figure 2. (a) SEM image of the MnO_x-5%ZrO₂ as representative sample; Energy Dispersive X-ray (EDX) spectra of MnO_x-10%ZrO₂ (b) and MnO_x-5%ZrO₂ (c). The EDX spectra were mediated considering four different zones of the samples.

Table 2. EDX elemental analysis of the examined samples. The presence of carbon was due to the carbon tape used to perform the measurements.

Sample	Element	wt. %
MnO _x -5%ZrO ₂	C	1.71
	O	28.32
	Mn	67.51
	Zr	2.46
MnO _x -10%ZrO ₂	C	1.23
	O	22.0
	Mn	67.66
	Zr	9.11

The surface valence state of the components of the catalysts were analysed through X-ray photoelectron spectroscopy (XPS) (Table 3). Interestingly, on the surface of MnO_x-based samples, the ratio of the Mn³⁺/Mn²⁺ ions obtained considering the area of the deconvoluted spectra (see Figure S2, spectra of MnO_x-5%ZrO₂ as representative sample) was the highest for the MnO_x-5%ZrO₂ mixed oxide. As pointed to also by the structural properties determined by XRD, in this sample, a strong ionic interaction between the Mn²⁺ and the Zn⁴⁺ was particularly favoured, leading to an increase in the amount of Mn³⁺ ions. Moreover, in this sample, the ratio between the surface lattice oxygen (O_α) located at about 530 eV and the chemisorbed/defective oxygen (O_β) at 532 eV was also the highest (Table 3, Figure S2), suggesting that the ionic exchange between the zirconium and the manganese ions also promoted a higher concentration of the manganese oxide surface oxygens. These, as reported, can participate in VOCs oxidation, improving the catalytic activity of the catalysts [24]. Finally, the binding energy of the Zr 3d_{5/2} at about 182.0 eV is the typical fingerprint of ZrO₂ [25]. The surface atomic percentage of Zr was 3.5 higher (2.77%) on the MnO_x-10%ZrO₂ compared to MnO_x-5%ZrO₂ (0.73%) confirming, as too stated by the EDX analysis, the surface covering of zirconia on manganese oxide, verified increasing the amount of ZrO₂.

Table 3. XPS analysis and binding energy (BE in eV) of the components of the investigated samples.

Sample	Mn 2p _{3/2} BE	Mn ³⁺ /Mn ²⁺ Ratio	Zr 3d _{5/2} BE	O 1s BE	O _α /O _β Ratio
Mn ₃ O ₄	641.2	0.52	182.1	529.8	1.50
ZrO ₂	/	/	182.0	529.9	1.48
MnO _x -5%ZrO ₂	640.9	0.69	181.9	529.9	1.69
MnO _x -10%ZrO ₂	641.1	0.55	182.0	530.0	1.53

The UV-DRS of the samples were reported in the Figure 3. The MnO_x-based samples (Figure 3a) showed a remarkable lower reflectance compared to the bare ZrO₂ (Figure 3b), and thus can be highlighted considering also the colours of the as-synthesized powders (dark brown for the MnO_x-based materials and white for the zirconium oxide). The optical bandgaps of the semiconductor oxides were estimated plotting the modified Kubelka–Munk function versus hv, as reported in the literature ([26], inset Figure 3b as representative sample). Interestingly, as established by XRD, the good crystallinity of ZrO₂ and its nano-size (8 nm, Table 1) allowed us to obtain a ZrO₂ with a lower bandgap (3.02 eV) compared to the other E_g reported in the literature for this oxide (about 5.0 eV that, however, can be narrowed down to 2–1.5 eV on the basis of the adopted preparation method [18,27]). No substantial variations were observed comparing the unmodified Mn₃O₄ and the MnO_x-ZrO₂ based-oxides, with an E_g of 3.26–3.29 eV (Table 1). Probably, the low amount and the good dispersion of ZrO₂ on MnO_x did not alter the bandgap of the manganese oxide. All the manganese oxide-based samples exhibited a similar E_g to TiO₂ (3.0–3.2 eV on the basis of the crystalline form [28]); thus, they can exploit the UV-A portion of solar irradiation.

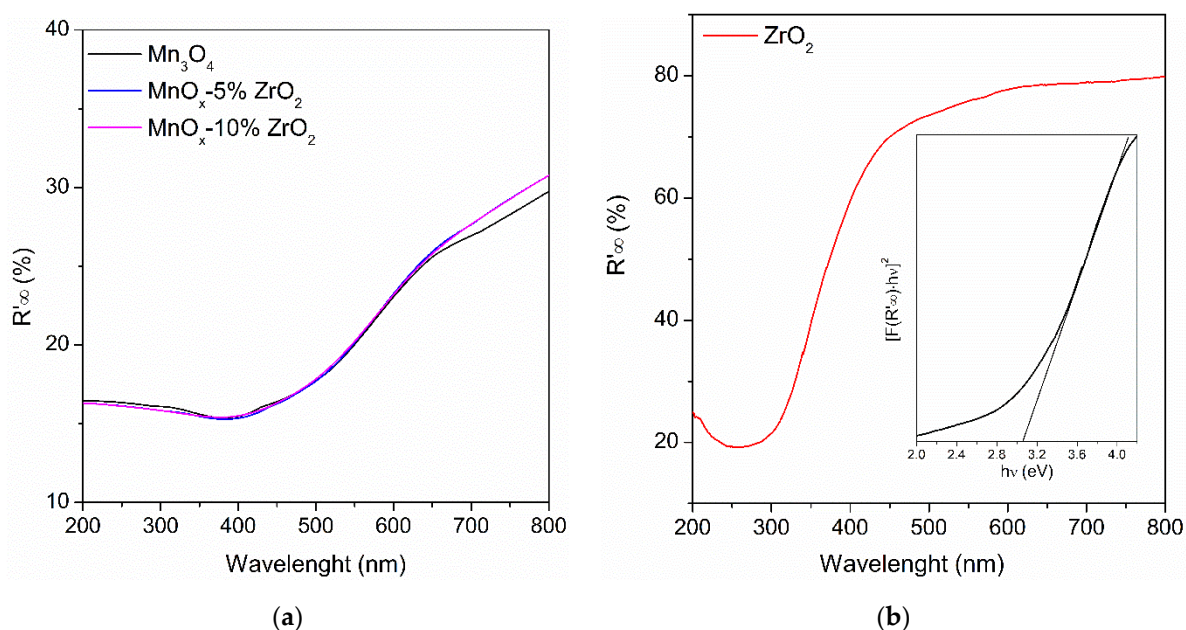


Figure 3. (a) UV-DRS (Diffuse Reflectance Spectroscopy) of the MnO_x -based samples; (b) UV-DRS spectra of bare ZrO_2 . In the inset; the estimation of the optical bandgap through the modified Kubelka–Munk function.

2.2. Photocatalytic, Thermocatalytic and Photothermo-Catalytic Removal of Toluene in Gas Phase

Figure 4a shows the solar photocatalytic activity in the oxidation of toluene at room temperature after 5 h of irradiation. The highest conversion value was obtained with the MnO_x -5% ZrO_2 (84%) followed by the MnO_x -10% ZrO_2 and the bare Mn_3O_4 (51% and 47%, respectively), whereas pure ZrO_2 exhibited the lowest conversion value (33%). In accordance with the literature [3,29], in our experimental condition, the only detected by-products were carbon dioxide and water with traces of benzaldehyde (selectivity in the range 1–3%). Although a real comparison with the other reported data for this reaction is very difficult, due to the various experimental conditions adopted by the other research groups (Table 4), the performance of MnO_x -5% ZrO_2 mixed oxide is very promising, being similar to (considering the initial concentration of 1000 ppm of toluene) or slightly lower than the most used TiO_2 -based photocatalysts, or to other unconventional semiconductors (Table 4).

Table 4. Data comparison of the photocatalytic oxidation of toluene.

Catalysts	Experimental Conditions	Toluene Conversion	Ref.
MnO_x -5% ZrO_2	1000 ppm Toluene, 5 h irradiation solar lamp (300 W, 10.7 mW/cm ²), room T, 150 mg catalyst	84%	this work
Brookite TiO_2 -5% CeO_2	1000 ppm Toluene, 2 h irradiation solar lamp (300 W, 10.7 mW/cm ²), room T, 150 mg catalyst	25%	[3]
TiO_2 - C_3N_4	665 ppm Toluene, 6 h irradiation, solar lamp (300 W, 612 mW/cm ²), 100 mg catalyst	93%	[30]
TiO_2 - MnO_2	200 ppmv Toluene, 1 h irradiation, 25 LEDs ($\lambda_{\text{max}} = 465 \text{ nm}$)	43%	[31]
0.5% Co/TiO_2	150 ppmv Toluene, 140 min irradiation, solar light (1000 mW/cm ²), 25 °C	96.5%	[32]
$\text{Ag}_4\text{Bi}_2\text{O}_5$	220 ppm Toluene, 60 min irradiation, Xe lamp with a 420 nm cut off filter (300 W, 0.25 mW/cm ²), 50 mg catalyst	93.1%	[33]
$\text{Fe}_2\text{O}_3/\text{In}_2\text{O}_3$	200 ppm Toluene, 8 h irradiation, Xenon lamp with an optical UV-cutoff filter (500 W, 40 mW/cm ²)	88.3%	[34]

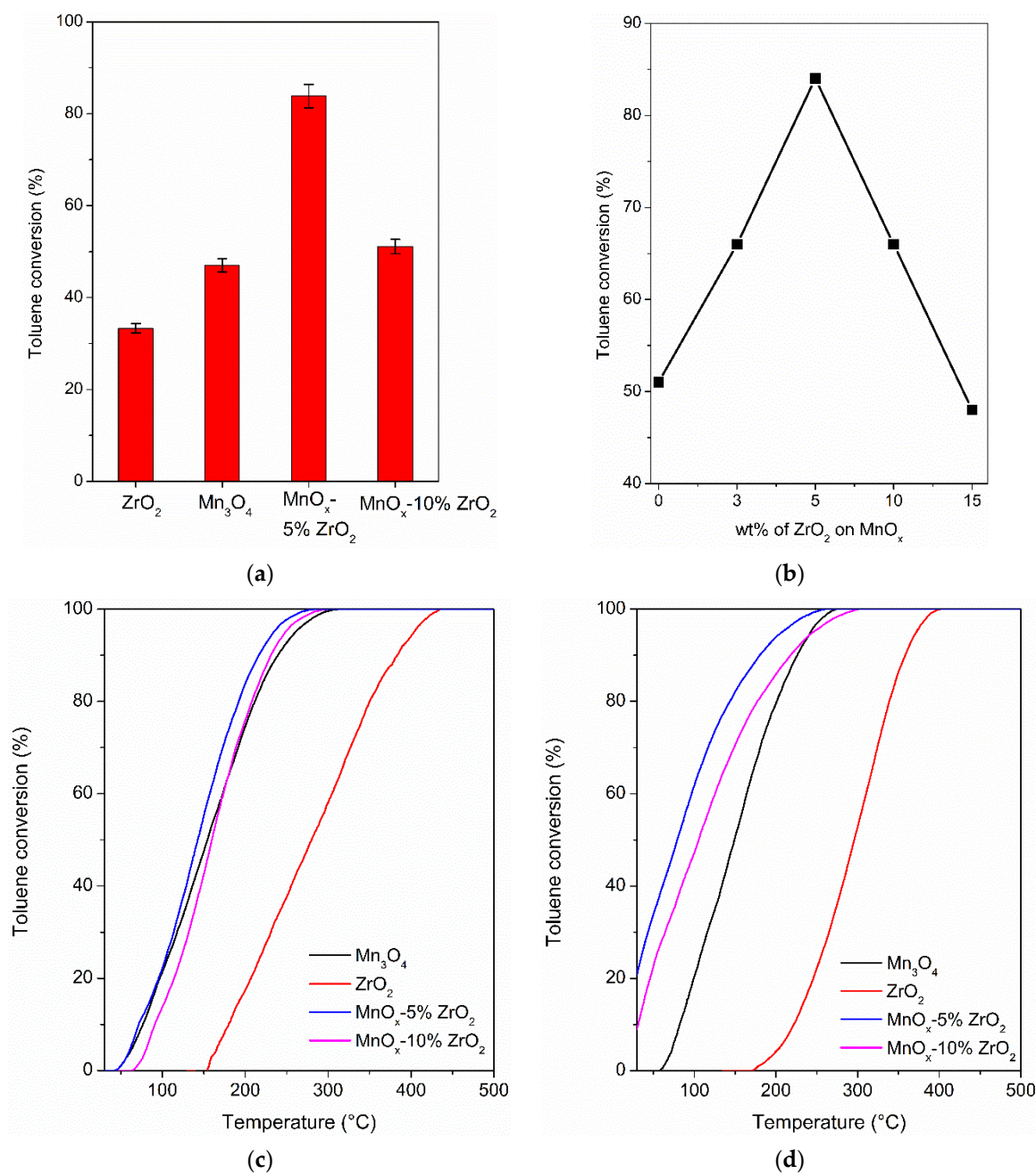


Figure 4. (a) Solar photocatalytic oxidation of toluene after 5h of irradiation; (b) effect of the wt.% of ZrO₂ on MnO_x in the solar photocatalytic toluene conversion; (c) thermocatalytic oxidation of toluene; (d) photothermo-catalytic oxidation of toluene on the investigated materials.

It is worth noting that 5 wt.% of zirconia was the best amount to obtain a synergistic positive effect on the MnO_x. Indeed, the samples prepared with the same procedures reported in the par. 4.1 but adding the 3 wt.% and 15 wt.% of zirconium oxide caused a decrease of activity (66% of toluene conversion for MnO_x-3% ZrO₂ and 48 % for MnO_x-15% ZrO₂, i.e., the same conversion value of the bare manganese oxide). The results pointed to a photocatalytic “volcano” trend (Figure 4b). The positive effects of the addition of ZrO₂ on MnO_x reached the maximum with 5% of zirconia, following a progressive decrease at higher amounts. This can be reasonably due, as confirmed by XRD, SEM-EDX and XPS measurements, to a progressive surface coverage of MnO_x, due to the presence of a large amount of ZrO₂. This caused a decrease in the photoactivity considering also the lower photocatalytic performance of bare ZrO₂ compared to manganese oxide (Figure 4a). The

detection of a specific amount of the hosted oxide on the main oxide is a typical trend of the mixed oxide-based semiconductors. A large amount of the second component (hosted oxide) can cover the surface active sites of the main oxide, decreasing the overall photocatalytic activity of the photocatalyst [35,36].

Thermal catalytic combustion is the most used process to increase the removal efficiency of toluene. The thermocatalytic activity of the investigated samples is reported in the Figure 4c. Moreover, for this catalytic approach, MnO_x -5% ZrO_2 gave the best results. The T_{90} (the temperature at which the 90% of toluene conversion was reached) values were 216 °C, 231 °C, 240 °C and 383 °C for MnO_x -5% ZrO_2 , MnO_x -10% ZrO_2 , Mn_3O_4 , and the bare ZrO_2 respectively, confirming the order of activity measured in the photocatalytic tests at room temperature.

To further decrease toluene T_{90} , the solar photothermo-catalytic tests were employed on the same investigated samples (Figure 4d). The solar-assisted thermo catalytic approach allowed one to decrease the T_{90} of 36 °C (180 °C) with respect to thermocatalytic tests on the best mixed oxide, the MnO_x -5% ZrO_2 catalyst, and in general, a decrease of T_{90} was verified for all the catalysts, with even the same order of activity: MnO_x -5% $\text{ZrO}_2 > \text{MnO}_x$ -10% ZrO_2 ($T_{90} = 217$ °C) $> \text{Mn}_3\text{O}_4$ ($T_{90} = 226$ °C) $> \text{ZnO}_2$ ($T_{90} = 245$ °C). Interestingly, the highest T_{90} decrease was verified with the bare zirconium oxide (138 °C lower compared to the thermocatalytic toluene T_{90}) where the activation of the zirconia photocatalytic properties was fundamental to promote the toluene total oxidation.

The positive synergistic effect due to the addition of a small amount of zirconia on the MnO_x and the solar multi-catalytic approach led to obtaining a low toluene T_{90} , considering the absence of noble metals co-catalysts. The obtained value of T_{90} with the MnO_x -5% ZrO_2 sample (180 °C) is comparable or lower with respect to the other MnO_x -based catalysts reported in the literature (in the range 200 °C–270 °C considering an initial toluene concentration of 1000 ppm [20,37]).

The influence of the gas hourly space velocity (GSHV) was reported in the Figure S3a considering the best sample (MnO_x -5% ZrO_2). We have chosen, for all the tests, a GSHV of 8×10^4 mL/ $\text{g}_{\text{cat}} \cdot \text{h}$, indeed, as expected, and as reported in the literature [38], with a high flow rate; the conversion rate of toluene to CO_2 and water (the only by-products detected also in all the thermo and photothermo-catalytic tests) was slower, whereas a $\text{GSHV} < 8 \times 10^4$ mL/ $\text{g}_{\text{cat}} \cdot \text{h}$ did not substantially modify the conversion rate.

2.3. Photocatalytic, Thermocatalytic and Photothermo-Catalytic Removal of Ethanol in Gas Phase

The ethanol being an alcohol was more reactive than the aromatic toluene, but its oxidation can give various by-products; the most common in the gas phase oxidation was acetaldehyde [3,31,39], which is also the main by-product detected in all the investigated catalytic approaches here discussed, whereas a very low selectivity (<2%) was detected in CO, formic acid, and acetic acid. In the solar photocatalytic tests, MnO_x -5% ZrO_2 confirmed its highest activity compared to the other samples (Figure 5) with an ethanol conversion of 98% and the highest selectivity to CO_2 (43%), the most important feature for the VOCs removal. The mixed oxide with the 10 wt.% of ZrO_2 showed a little decrease of photoactivity (ethanol conversion of 86%) and a higher selectivity to acetaldehyde (60%) with respect to CO_2 (36%). These data, in line with the photo-oxidation of toluene (Figure 4a), pointed to, in our experimental conditions, the 5 wt.% being the optimal amount of zirconia to have a synergistic effect with MnO_x . Among the bare oxides, the manganese oxide showed a higher ethanol conversion, with a higher selectivity to CO_2 compared to ZrO_2 . This latter oxide promoted the partial oxidation to acetaldehyde (selectivity of 74%) and consequently exhibited the lowest selectivity to CO_2 (22%).

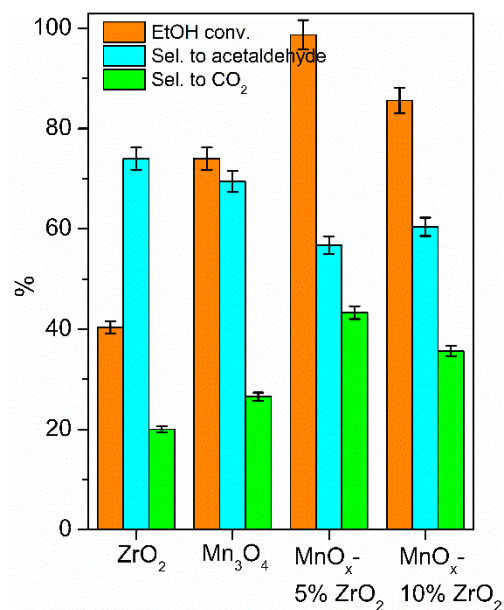


Figure 5. Solar photocatalytic oxidation of ethanol after 5 h of irradiation.

In Table 5 and Figure S4, the data of the thermocatalytic oxidation of ethanol are reported. MnO_x-5%ZrO₂ showed, also for this VOC, the best performance, with the lowest T₉₀ (189 °C) and a maximum conversion to acetaldehyde of 66% at 176 °C. Moreover, MnO_x-10%ZrO₂ and Mn₃O₄ showed the same maximum conversion to acetaldehyde, but at a higher temperature (200 °C for MnO_x-10%ZrO₂ and 226 °C for bare manganese oxide). Consequently, MnO_x-5%ZrO₂ also exhibited the lowest T₉₀ related to the conversion to CO₂ (361 °C). It is verified also for this approach, a little negative effect of the increased amount of zirconium oxide on the MnO_x, with higher T₉₀ of MnO_x-10%ZrO₂ compared to MnO_x-5%ZrO₂. The highest conversion to acetaldehyde was obtained with the bare zirconia (maximum conversion of 98% at 409 °C) confirming, as also detected in the photocatalytic tests at room temperature, the tendency of this catalyst to promote the partial oxidation of ethanol instead of the total combustion.

Table 5. Data of the thermocatalytic oxidation of ethanol on the investigated samples.

Sample	Ethanol Conversion	Conversion to CO ₂	Maximum Conversion to Acetaldehyde
Mn ₃ O ₄	T ₁₀ = 95 °C T ₅₀ = 167 °C T ₉₀ = 239 °C	T ₁₀ = 217 °C T ₅₀ = 299 °C T ₉₀ = 411 °C	65% (226 °C)
ZrO ₂	T ₁₀ = 221 °C T ₅₀ = 292 °C T ₉₀ = 382 °C	T ₁₀ = 428 °C T ₅₀ = 453 °C T ₉₀ = 474 °C	98% (409 °C)
MnO _x -5%ZrO ₂	T ₁₀ = 45 °C T ₅₀ = 116 °C T ₉₀ = 189 °C	T ₁₀ = 167 °C T ₅₀ = 249 °C T ₉₀ = 361 °C	66% (176 °C)
MnO _x -10%ZrO ₂	T ₁₀ = 70 °C T ₅₀ = 141 °C T ₉₀ = 214 °C	T ₁₀ = 182 °C T ₅₀ = 264 °C T ₉₀ = 376 °C	66% (200 °C)

Interestingly also for the removal of ethanol, the multi-catalytic reaction (i.e., the photothermo-catalysis) allowed us to improve the performance related to ethanol oxidation (Table 6, Figure S5). With MnO_x-5%ZrO₂, the T₉₀ of ethanol conversion was lowered

to 34 °C (154 °C), a value that is comparable or lower, considering an initial ethanol concentration of 1000 ppm, with respect to the other MnO_x-based materials reported in the literature (in the range 127 °C (initial ethanol concentration of 300 ppm) –200 °C (initial ethanol concentration of 600–1945 ppm) [37,40]). The total oxidation to CO₂ was favoured on this sample, and for this reason, the maximum conversion to acetaldehyde was low (35% at 118 °C), with a decrease of 205 °C of the T₉₀ related to the conversion to CO₂ compared to the thermocatalytic tests.

Table 6. Data of the photothermo-catalytic oxidation of ethanol on the investigated samples.

Sample	Ethanol Conversion	Conversion to CO ₂	Maximum Conversion to Acetaldehyde
Mn ₃ O ₄	T ₁₀ = 48 °C T ₅₀ = 126 °C T ₉₀ = 214 °C	T ₁₀ = 150 °C T ₅₀ = 249 °C T ₉₀ = 367 °C	58% (187 °C)
ZrO ₂	T ₁₀ = 205 °C T ₅₀ = 277 °C T ₉₀ = 369 °C	T ₁₀ = 397 °C T ₅₀ = 437 °C T ₉₀ = 476 °C	91% (378 °C)
MnO _x -5%ZrO ₂	T ₁₀ = 51 °C T ₅₀ = 123 °C T ₉₀ = 154 °C	T ₁₀ = 119 °C T ₅₀ = 137 °C T ₉₀ = 156 °C	35% (118 °C)
MnO _x -10%ZrO ₂	T ₁₀ = 74 °C T ₅₀ = 145 °C T ₉₀ = 204 °C	T ₁₀ = 123 °C T ₅₀ = 165 °C T ₉₀ = 207 °C	24% (127 °C)

A further decrease of the maximum conversion to acetaldehyde was verified with MnO_x-10%ZrO₂ (24%), but at a higher temperature (127 °C) compared to the MnO_x-5%ZrO₂, confirming that, with these mixed oxides, the combustion of ethanol was favoured with respect to its partial oxidation. For all the tested samples, similar to the photothermal oxidation of toluene, there was a positive effect of the solar light irradiation, with a contextual decrease of conversion temperatures compared to the thermocatalytic tests (comparison between Tables 5 and 6). The unmodified zirconia remained the less active catalyst, however, the solar-assisted reaction decreased T₉₀ of ethanol conversion of 13 °C compared to the tests without irradiation.

3. Discussion

The mixed oxides MnO_x-ZrO₂ here investigated showed promising performance in the removal of VOCs in the gas phase, considering the absence of noble metals co-catalysts and an initial VOCs concentration of 1000 ppm. The amount of zirconium oxide added on manganese oxide is a key parameter to improve the catalytic and the photocatalytic performance. The as-synthesized samples showed a comparable optical bandgap, in the range 3.0–3.3 eV (Table 1), similar to the TiO₂, and able to exploit the UV-A portion of the solar light. The addition of zirconia on manganese oxide led to a slight decrease of the surface area (Table 1) that, however, did not comprise the catalytic activity of the mixed oxides.

The presence of a small amount of zirconium oxide on MnO_x allowed, as stated by XRD and SEM-EDX, an ionic exchange between Zr⁴⁺ and Mn²⁺; this favoured the formation of a synergistic effect between the two oxides, with structural changes in the bulk of MnO_x. These modifications led to increasing the (photo)catalytic activity compared to the bare oxides. Indeed, when reducible oxides, i.e., which own mobile/reducible oxygens, were used for the oxidation of VOCs, the total oxidation to CO₂ is favoured, because these oxygens can participate in the reaction with a Mars–Van Krevelen (MvK) mechanism [41,42]. The oxygen vacancies on the surface of the oxide will be subsequently filled by the O₂ present in the gas phase.

This mechanism was boosted up with the photothermo-catalytic approach because the photocatalytic mechanism generated the superoxide ($O_2^{\bullet-}$) and hydroxyl (OH^{\bullet}) radicals [43,44], that being more reactive of the molecular O_2 , increased the rate of the total oxidation of VOCs (reactions a–i, Figure 6) and the re-filling of the oxygen vacancies, being the mobile oxygens of MnO_x activated by the heating [13,45]. For these reasons, the conversion temperatures of both toluene and ethanol oxidation were sensibly lower compared to the thermocatalysis, especially with the MnO_x -5% ZrO_2 sample. In this way, it was possible to exploit a double positive effect: (i) the solar irradiation effect: that allowed the formation of more reactive species, (ii) the thermal effect: that activated the redox mobility of the manganese oxide oxygens [13,20,45].

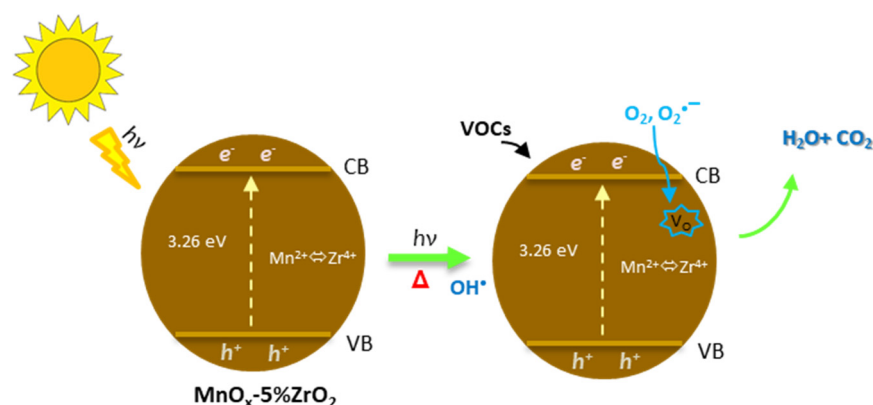


Figure 6. Proposed photothermo-catalytic mechanism. V_o = oxygen vacancy.

Photothermo-catalytic mechanism:

- (i) *Solar irradiation effect (VB and CB indicate the valence and the conduction bands):*
 - (a) Charge carriers formation: MnO_x -5% $ZrO_2 + hv(\text{solar}) \rightarrow MnO_x$ -5% $ZrO_2 (h\nu_{VB}^+ + e^-_{CB})$
 - (b) Formation of hydroxyl radical: $h^+_{VB} + H_2O(g) \rightarrow OH^{\bullet} + H^+_{aq}$
 - (c) Formation of superoxide radical: $e^-_{CB} + O_2 \rightarrow O_2^{\bullet-}$
- (ii) *Thermal effect (V_o = oxygen vacancy)*
 - (d) Oxygen from the mixed oxide: MnO_x -5% $ZrO_2 \rightarrow MnO_x$ -5% $ZrO_2 (V_o) + 1/2 O_2(g)_{\text{from oxide}}$
 - (e) VOC oxidation: $VOC + O_2(g) + O_2(g)_{\text{from oxide}} \xrightarrow{\text{heat}} CO_2 + H_2O$
 - (f) Oxygen restoring: MnO_x -5% $ZrO_2 (V_o) + 1/2 O_2(g) \rightarrow MnO_x$ -5% ZrO_2
- (iii) *Solar photothermal effect*
 - (g) MnO_x -5% $ZrO_2 + hv \xrightarrow{\text{heat}} MnO_x$ -5% $ZrO_2 (V_o) + 1/2 O_2(g)_{\text{from oxide}} + OH^{\bullet} + O_2^{\bullet-}$
 - (h) Improved VOC oxidation: $VOC + O_2(g) + O_2(g)_{\text{from oxide}} + OH^{\bullet} + O_2^{\bullet-} \rightarrow CO_2 + H_2O$
 - (i) Oxygen speeded up restoring: MnO_x -5% $ZrO_2 (V_o) + 1/2 O_2(g) + O_2^{\bullet} \rightarrow MnO_x$ -5% ZrO_2

It is worth noting that the reactions (a–c) and (d–f) are also involved in the solar photocatalysis at room temperature and in the bare thermocatalytic tests, respectively. The multi-catalytic effect (reactions g–i) allowed one to increase the performance and to favour the total oxidation of the employed VOCs to CO_2 .

Another confirmation of the proposed MvK mechanism was reported in the Figure S3b. In the photothermo-catalytic oxidation of toluene with the MnO_x -5% ZrO_2 sample, the air (more interesting from a practical point of view) was replaced in the gas mixture with the pure oxygen. It is possible to note that the presence of oxygen led to a beneficial effect for the toluene conversion to CO_2 , being the T_{90} lower of 25 °C (155 °C) compared to the test with air (180 °C). This can be reasonably ascribed to the easier oxygen restoring on

the catalyst surface (reaction i), in an oxygen-rich environment, favouring, in this way, the MvK route.

As stated by the characterization data, the good interaction between the manganese and zirconium oxide (especially at low amount of ZrO_2) improved the photothermo-catalytic mechanism with the redox process on MnO_x that was favoured by the ionic exchange between the zirconium and the manganese ions. On the contrary, an increased amount of zirconium oxide led to a progressive deposition of the hosted oxide on the surface of MnO_x covering, in this way, the surface-active sites of manganese oxide [35,36]. For these reasons, the optimal performance was obtained with 5 wt.% of ZrO_2 . In this contest, the mobility of the surface oxygens of the MnO_x -5% ZrO_2 sample was favoured by the MnO_x redox properties, and consequently, it is strictly related to its reducibility. Furthermore, the amount of the surface oxygens on MnO_x -5% ZrO_2 was higher compared to the other samples, as detected by XPS. To have a further confirmation of the high reducibility/mobility of the surface oxygens of MnO_x -5% ZrO_2 , the H_2 -temperature-programmed reduction (TPR) measurements were carried out, and the sample profiles were reported in Figure 7. In accordance with the literature data [20,46], the TPR profiles of the MnO_x -based samples were characterized to broad reduction peaks, due to the occurrence of several reduction processes of the Mn ions. As expected, the MnO_x -5% ZrO_2 sample showed the lowest reduction feature (201 °C) attributed to the reduction of Mn_2O_3 to Mn_3O_4 [46], 111 °C and 117 °C lower compared to the same reduction feature of Mn_3O_4 and MnO_x -10% ZrO_2 , respectively. This reduction peak was also more intense for the MnO_x -5% ZrO_2 compared to the other MnO_x -based samples confirming, as detected by XRD and XPS, the major presence of Mn^{3+} ions on MnO_x -5% ZrO_2 . The higher temperature reduction signals in the range 300–480° were ascribed to the further reduction of Mn_3O_4 to MnO [46]. Moreover, in this case, the sample with 5 wt.% of ZrO_2 showed the highest reducibility (i.e., the lowest peak temperature). This is connected to the highest mobility/reducibility of the surface oxygens of MnO_x -5% ZrO_2 , which favours the MvK mechanism, and therefore a better VOCs abatement. The reduction temperature of bare ZrO_2 started at a temperature above 500 °C [47], and for this reason, in our analysis (in the range 50–550°C), its reduction peak was not complete.

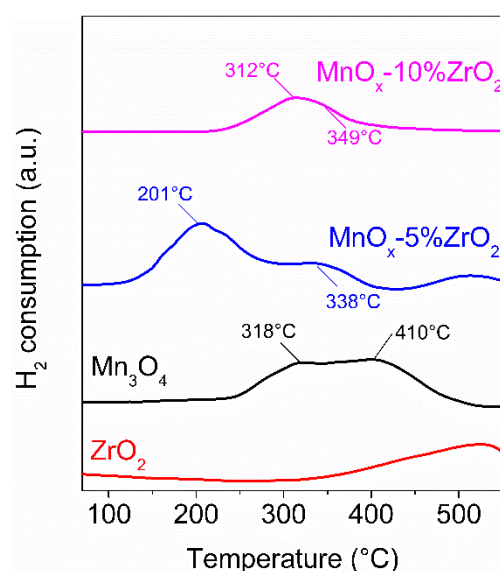


Figure 7. H_2 -TPR (Temperature programmed reduction) profiles of the investigated samples.

Between the photocatalytic, the thermocatalytic and the photothermo-catalytic removal of VOCs, although the solar photocatalytic reaction has the advantages of work at room temperature and that with the MnO_x -5% ZrO_2 , it reached a similar activity of the most used TiO_2 -based materials (Table 4); to have a complete VOCs removal, it is necessary

to have contextual heating. For this purpose, the solar photothermo-catalysis can be an optimal solution to obtain the good performance of the thermocatalysis, but with an energy saving, due to the lower temperature required for the VOCs conversion. Indeed, the best sample ($\text{MnO}_x\text{-5\%ZrO}_2$) tested in our experimental conditions showed a decrease of $36\text{ }^\circ\text{C}$ and $34\text{ }^\circ\text{C}$ of the toluene and ethanol T_{90} conversion compared to the thermocatalytic tests favouring in both the reactions; the total oxidation to CO_2 (the T_{90} of ethanol conversion to CO_2 was lowered of $205\text{ }^\circ\text{C}$, Tables 5 and 6).

Finally, the stability in the time-on steam toluene removal of $\text{MnO}_x\text{-5\%ZrO}_2$ was good (Figure 8, toluene solar photothermo-oxidation) and pointed to the $\text{MnO}_x\text{-ZrO}_2$ catalyst being a promising versatile material for application in thermocatalysis, photocatalysis, and photothermo-catalysis.

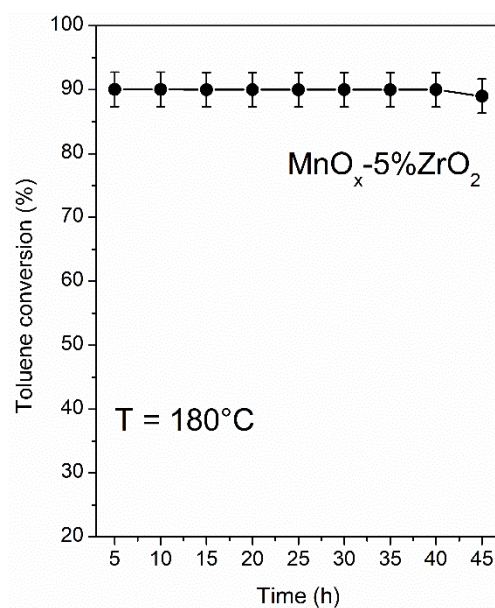


Figure 8. Stability test of $\text{MnO}_x\text{-5\%ZrO}_2$ catalyst in the toluene solar photothermo-catalytic oxidation.

4. Materials and Methods

4.1. Catalysts Synthesis

Bare manganese oxide was prepared by chemical precipitation with NaOH (1 M) (Panreac Química SLU, Castellar del Vallès (Barcelona), Spain). In particular, a certain amount of manganese (II) chloride tetrahydrate (Sigma-Aldrich, Buchs, Switzerland) was dissolved in demineralized water and heated at $70\text{ }^\circ\text{C}$. After the NaOH was added dropwise until the $\text{pH} = 10$. Successively, the solution was stirred and kept at $70\text{ }^\circ\text{C}$ for 2 h. After digestion for 24 h, the slurry was filtered and dried at $120\text{ }^\circ\text{C}$ overnight. Finally, the resultant powders were calcined in air at $600\text{ }^\circ\text{C}$ for 2 h.

A similar procedure was followed for the bare ZrO_2 . In this case, the zirconyl nitrate hydrate (Fluka, Buchs, Switzerland) and ammonia (as precipitant agent, 25–28%, Sigma-Aldrich, Buchs, Switzerland) were used, following the same procedures reported above, and the same thermal treatments (drying at $120\text{ }^\circ\text{C}$, and calcination at $600\text{ }^\circ\text{C}$ for 2 h).

For the $\text{MnO}_x\text{-ZrO}_2$ mixed oxides, the NaOH -driven precipitation was employed using the required stoichiometric amount of zirconyl nitrate hydrate to obtain the chosen nominal concentration in weight percentage (wt.%) of ZrO_2 . Moreover, in this case, the samples were dried at $120\text{ }^\circ\text{C}$ and calcined in air at $600\text{ }^\circ\text{C}$ for 2 h.

4.2. Catalysts Characterization

The sample structures were determined through the X-ray powder diffraction (XRD) using a Smartlab Rigaku diffractometer (Rigaku Europe SE, Hugenottenallee 167 Neu-Isenburg 63263, Germany) in Bragg–Brentano mode, equipped with a rotating anode of Cu

K α radiation operating at 45 kV and 200 mA. The surface morphology was examined with field emission scanning electron microscopy (FE-SEM) using a ZEISS SUPRA 55 VP (Carl Zeiss QEC GmbH, Garching b. München, Germany). The composition of the powders was carried out by the energy dispersive X-ray (EDX) analysis using an INCA-Oxford (Oxford Instruments plc, Tubney Woods, Abingdon, Oxfordshire, United Kingdom) windowless detector, and a resolution of 127 eV determined using the half-height amplitude (FWHM) of the K α of Mn.

The BET surface area values were determined by N₂ adsorption–desorption measurements with a Sorptomatic 1990 instrument (Thermo Quest, Milano, Italy). Before the measurements, the catalysts were outgassed overnight at 200 °C.

The UV-vis Diffuse Reflectance spectra (UV-Vis DRS, Diffuse Reflectance Spectroscopy) measurements were performed with a Jasco V- 670 spectrometer (Jasco Europe S.R.L., Cremella, Italy) provided with an integration sphere and using barium sulphate (Fluka, Buchs, Switzerland) as standard. The estimation of the optical band gap of the samples was determined using the Kubelka–Munch function [26].

The X-ray photoelectron spectroscopy (XPS) was performed with a K-alpha X-ray photoelectron instrument (Thermo Fisher Scientific, Waltham, MA, USA), employing the C 1s peak at 284.9 eV (of adventitious carbon) as reference.

The H₂-TPR (Temperature programmed reduction) profiles of the samples were obtained using a home-made flow equipment (gas-mixture 5 vol.% H₂ in Ar) and a TCD detector, following the procedures reported in ref. [48].

4.3. Photo, Thermo and Photothermo-Catalytic Oxidation of VOCs

The thermocatalytic removal of VOCs in gas phase and atmospheric pressure was carried out in a fixed bed flow reactor packed with the powder catalysts (0.15 g, 80–140 mesh), using the same experimental conditions described in the ref. [3]. A heating ramp of 10 °C was used in all the tests from room temperature to 500 °C. To assure a steady-state before the catalytic measurements, the gas mixture (1000 ppm VOCs; 10 vol.% air, rest He) was flowed on the catalyst for 30 min. No substantial contribution due to the adsorption process was detected. The reaction products were analysed by a gas chromatography (Smart-IQ+ Thermo Onix, Thermo Fisher Scientific 168 Third Avenue, Waltham, MA, USA 0245) utilizing a packed column with 10% FFAP on Chromosorb W (from Merck KGaA, Darmstadt, Germany) with a FID (Flame Ionization Detector), coupled with a quadrupole mass spectrometer (VG quadropoles, Fergutec B.V. Dragonder 13 C, 5554 GM Valkenswaard, The Netherlands).

The photocatalytic and the photothermo-catalytic tests were performed with the same instruments described above. The simultaneous irradiation in the photothermo-catalytic tests was made with an artificial solar lamp (OSRAM Vitalux 300 W, 10.7 mW/cm², OSRAM Opto Semiconductors GmbH, Leibniz, Regensburg Germany). In the photocatalytic tests, a fan located near the reactor allowed us to maintain a constant temperature, avoiding the overheating effects due to lamp emission.

5. Conclusions

The MnO_x-ZrO₂ mixed oxides exhibited promising performance in the removal of toluene and ethanol in the gas phase, especially in the multi-catalytic solar photothermal approach. The ionic interaction between the manganese and the zirconium ions exploited with the addition of a low amount of zirconium oxide allowed us to boost up the Mars–van Krevelen mechanism of the VOCs oxidation favouring the total oxidation of VOCs to CO₂. Furthermore, with the photothermo-catalysis, a decrease of the conversion temperatures compared to the thermocatalysis was verified, and MnO_x-5 wt.%ZrO₂ also showed good stability. Finally, with the same catalyst in the solar photocatalytic tests at room temperature, a similar activity of the most used TiO₂-based materials was obtained, pointing to the fact that this sample can be promising for the VOCs remediation technologies, being cheaper, not critical, and performing considering the absence of noble metal co-catalysts.

Supplementary Materials: The following supporting information can be downloaded at: <https://www.mdpi.com/article/10.3390/catal12010085/s1>, Figure S1: SEM images of the other investigated samples; Figure S2: XPS characterization of the MnO_x-5% ZrO₂ sample; Figure S3: Photothermo-catalytic oxidation of toluene: influence of different parameters on MnO_x-5% ZrO₂ sample; Figure S4: thermocatalytic oxidation of ethanol; Figure S5: Photothermo-catalytic oxidation of ethanol.

Author Contributions: Conceptualization, R.F.; investigation, R.A.F., R.F., F.L.P., E.M.M., S.A.B.; writing—original draft preparation, R.F.; writing—review and editing, R.F.; supervision, R.F. All authors have read and agreed to the published version of the manuscript.

Funding: This research received no external funding.

Data Availability Statement: The data presented in this study are available on request from the corresponding author.

Acknowledgments: The authors thank S. Scirè (University of Catania) for the use of the laboratory facilities and the Bio-nanotech Research and Innovation Tower (BRIT) laboratory of the University of Catania for the Smartlab diffractometer facility. R.F. thanks the PON “AIM” of the European Social Found for the support.

Conflicts of Interest: The authors declare no conflict of interest.

References

1. Li, Y.; Wu, S.; Wu, J.; Hu, Q.; Zhou, C. Photothermocatalysis for efficient abatement of CO and VOCs. *J. Mater. Chem. A* **2020**, *8*, 8171–8194. [[CrossRef](#)]
2. Boyjoo, Y.; Sun, H.; Liu, J.; Pareek, V.K.; Wang, S. A review on photocatalysis for air treatment: From catalyst development to reactor design. *Chem. Eng. J.* **2017**, *310*, 537–559. [[CrossRef](#)]
3. Bellardita, M.; Fiorenza, R.; D’Urso, L.; Spitaleri, L.; Gulino, A.; Compagnini, G.; Scirè, S.; Palmisano, L. Exploring the photothermo-catalytic performance of brookite TiO₂-CeO₂ composites. *Catalysts* **2020**, *10*, 765. [[CrossRef](#)]
4. Ma, R.; Sun, J.; Li, D.H.; Wei, J.J. Review of synergistic photo-thermo-catalysis: Mechanisms, materials and applications. *Int. J. Hydrogen Energy* **2020**, *45*, 30288–30324. [[CrossRef](#)]
5. Keller, N.; Ivanez, J.; Highfield, J.; Ruppert, A.M. Photo-/thermal synergies in heterogeneous catalysis: Towards low-temperature (solar-driven) processing for sustainable energy and chemicals. *Appl. Catal. B Environ.* **2021**, *296*, 120320. [[CrossRef](#)]
6. Abidi, M.; Assadi, A.A.; Bouzaza, A.; Hajjaji, A.; Bessais, B.; Rtimi, S. Photocatalytic indoor/outdoor air treatment and bacterial inactivation on Cu_xO/TiO₂ prepared by HiPIMS on polyester cloth under low intensity visible light. *Appl. Catal. B Environ.* **2019**, *259*, 118074. [[CrossRef](#)]
7. Li, Q.; Li, F. Recent advances in surface and interface design of photocatalysts for the degradation of volatile organic compounds. *Adv. Colloid Interface Sci.* **2020**, *284*, 102275. [[CrossRef](#)]
8. Zhang, S.; Pu, W.; Chen, A.; Xu, Y.; Wang, Y.; Yang, C.; Gong, J. Oxygen vacancies enhanced photocatalytic activity towards VOCs oxidation over Pt deposited Bi₂WO₆ under visible light. *J. Hazard. Mater.* **2020**, *384*, 121478. [[CrossRef](#)] [[PubMed](#)]
9. Fiorenza, R.; Bellardita, M.; Balsamo, S.A.; Spitaleri, L.; Gulino, A.; Condorelli, M.; D’Urso, L.; Scirè, S.; Palmisano, L. A solar photothermocatalytic approach for the CO₂ conversion: Investigation of different synergisms on CoO-CuO/brookite TiO₂-CeO₂ catalysts. *Chem. Eng. J.* **2022**, *428*, 131249. [[CrossRef](#)]
10. Lewicka, E.; Guzik, K.; Galos, K. On the possibilities of critical raw materials production from the EU’s primary sources. *Resources* **2021**, *10*, 50. [[CrossRef](#)]
11. Fiorenza, R. Bimetallic catalysts for volatile organic compound oxidation. *Catalysts* **2020**, *10*, 661. [[CrossRef](#)]
12. Ristig, S.; Cibura, N.; Strunk, J. Manganese oxides in heterogeneous (photo)catalysis: Possibilities and challenges. *Green* **2015**, *5*, 23–41. [[CrossRef](#)]
13. Feng, Y.; Wang, C.; Wang, C.; Huang, H.; Hsi, H.-C.; Duan, E.; Liu, Y.; Guo, G.; Dai, H.; Deng, J. Catalytic stability enhancement for pollutant removal via balancing lattice oxygen mobility and VOCs adsorption. *J. Hazard. Mater.* **2022**, *424*, 127337. [[CrossRef](#)] [[PubMed](#)]
14. Cai, T.; Liu, Z.; Yuan, J.; Xu, P.; Zhao, K.; Tong, Q.; Lu, W.; He, D. The structural evolution of MnO_x with calcination temperature and their catalytic performance for propane total oxidation. *Appl. Surf. Sci.* **2021**, *565*, 150596. [[CrossRef](#)]
15. Yang, R.; Fan, Y.; Ye, R.; Tang, Y.; Cao, X.; Yin, Z.; Zeng, Z. MnO₂-based materials for environmental applications. *Adv. Mater.* **2021**, *33*, 1–53.
16. Kondratowicz, T.; Drozdek, M.; Michalik, M.; Gac, W.; Gajewska, M.; Kuśtrowski, P. Catalytic activity of Pt species variously dispersed on hollow ZrO₂ spheres in combustion of volatile organic compounds. *Appl. Surf. Sci.* **2020**, *513*, 145788. [[CrossRef](#)]
17. Scirè, S.; Liotta, L.F. Supported gold catalysts for the total oxidation of volatile organic compounds. *Appl. Catal. B Environ.* **2012**, *125*, 222–246. [[CrossRef](#)]
18. Hassan, N.S.; Jalil, A.A. A review on self-modification of zirconium dioxide nanocatalysts with enhanced visible-light-driven photodegradation of organic pollutants. *J. Hazard. Mater.* **2022**, *423*, 126996. [[CrossRef](#)] [[PubMed](#)]

19. Chen, G.; Wang, Z.; Lin, F.; Zhang, Z.; Yu, H.; Yan, B.; Wang, Z. Comparative investigation on catalytic ozonation of VOCs in different types over supported MnO catalysts. *J. Hazard. Mater.* **2020**, *391*, 122218. [[CrossRef](#)] [[PubMed](#)]
20. Huang, X.; Li, L.; Liu, R.; Li, H.; Lan, L.; Zhou, W. Optimized synthesis routes of MnO_x-ZrO₂ hybrid catalysts for improved toluene combustion. *Catalysts* **2021**, *11*, 1037. [[CrossRef](#)]
21. González, U.; Schifter, I.; Díaz, L.; González-Macías, C.; Mejía-Centeno, I.; Sánchez-Reyna, G. Assessment of the use of ethanol instead of MTBE as an oxygenated compound in Mexican regular gasoline: Combustion behavior and emissions. *Environ. Monit. Assess.* **2018**, *190*, 700. [[CrossRef](#)]
22. Niu, X.; Wei, H.; Tang, K.; Liu, W.; Zhao, G.; Yang, Y. Solvothermal synthesis of 1D nanostructured Mn₂O₃: Effect of Ni²⁺ and Co²⁺ substitution on the catalytic activity of nanowires. *RSC Adv.* **2015**, *5*, 66271–66277. [[CrossRef](#)]
23. Gutiérrez-Ortiz, J.I.; de Rivas, B.; López-Fonseca, R.; Martín, S.; González-Velasco, J.R. Structure of Mn–Zr mixed oxides catalysts and their catalytic performance in the gas-phase oxidation of chlorocarbons. *Chemosphere* **2007**, *68*, 1004–1012. [[CrossRef](#)] [[PubMed](#)]
24. Santos, V.P.; Pereira, M.F.R.; Órfão, J.J.M.; Figueiredo, J.L. The role of lattice oxygen on the activity of manganese oxides towards the oxidation of volatile organic compounds. *Appl. Catal. B Environ.* **2010**, *99*, 353–363. [[CrossRef](#)]
25. Zeng, K.; Li, X.; Wang, C.; Wang, Z.; Guo, P.; Yu, J.; Zhang, C.; Zhao, X.S. Three-dimensionally macroporous MnZrO catalysts for propane combustion: Synergistic structure and doping effects on physicochemical and catalytic properties. *J. Colloid Interface Sci.* **2020**, *572*, 281–296. [[CrossRef](#)] [[PubMed](#)]
26. López, R.; Gómez, R. Band-gap energy estimation from diffuse reflectance measurements on sol–gel and commercial TiO₂: A comparative study. *J. Sol-Gel Sci. Technol.* **2012**, *61*, 1–7. [[CrossRef](#)]
27. Mishra, S.; Debnath, A.; Muthe, K.; Das, N.; Parhi, P. Rapid synthesis of tetragonal zirconia nanoparticles by microwave-solvothermal route and its photocatalytic activity towards organic dyes and hexavalent chromium in single and binary component systems. *Colloids Surf. A Physicochem. Eng. Asp.* **2021**, *608*, 125551. [[CrossRef](#)]
28. Yamakata, A.; Vequizo, J.J.M. Curious behaviors of photogenerated electrons and holes at the defects on anatase, rutile, and brookite TiO₂ powders: A review. *J. Photochem. Photobiol. C Photochem. Rev.* **2019**, *40*, 234–243. [[CrossRef](#)]
29. Maira, A.J.; Yeung, K.L.; Soria, J.; Coronado, J.M.; Bolver, C.; Lee, C.Y.; Augugliaro, V. Gas-phase photo-oxidation of toluene using nanometer-size TiO₂ catalysts. *Appl. Catal. B Environ.* **2001**, *29*, 327–336. [[CrossRef](#)]
30. Yu, J.; Caravaca, A.; Guillard, C.; Vernoux, P.; Zhou, L.; Wang, L.; Lei, J.; Zhang, J.; Liu, Y. Carbon nitride quantum dots modified TiO₂ inverse opal photonic crystal for solving indoor vocs pollution. *Catalysts* **2021**, *11*, 464. [[CrossRef](#)]
31. Nevárez-Martínez, M.C.; Kobylanski, M.P.; Mazierski, P.; Wólkiewicz, J.; Trykowski, G.; Malankowska, A.; Kozak, M.; Espinoza-Montero, P.J.; Zaleska-Medynska, A. Self-organized TiO₂-MnO₂ nanotube arrays for efficient photocatalytic degradation of toluene. *Molecules* **2017**, *22*, 564. [[CrossRef](#)] [[PubMed](#)]
32. Almomani, F.; Bhosale, R.; Shawaqfah, M. Solar oxidation of toluene over Co doped nano-catalyst. *Chemosphere* **2020**, *255*, 126878. [[CrossRef](#)]
33. Chen, A.; Chen, G.; Wang, Y.; Lu, Y.; Chen, J.; Gong, J. Fabrication of novel Ag₄Bi₂O_{5-x} towards excellent photocatalytic oxidation of gaseous toluene under visible light irradiation. *Environ. Res.* **2021**, *197*, 111130. [[CrossRef](#)]
34. Zhang, F.; Li, X.; Zhao, Q.; Zhang, Q.; Tadó, M.; Liu, S. Fabrication of α-Fe₂O₃/In₂O₃ composite hollow microspheres: A novel hybrid photocatalyst for toluene degradation under visible light. *J. Colloid Interface Sci.* **2015**, *457*, 18–26. [[CrossRef](#)] [[PubMed](#)]
35. Khanmohammadi, M.; Shahrouzi, J.R.; Rahmani, F. Insights into mesoporous MCM-41-supported titania decorated with CuO nanoparticles for enhanced photodegradation of tetracycline antibiotic. *Environ. Sci. Pollut. Res.* **2021**, *28*, 862–879. [[CrossRef](#)]
36. Fiorenza, R.; Bellardita, M.; Scirè, S.; Palmisano, L. Effect of the addition of different doping agents on visible light activity of porous TiO₂ photocatalysts. *Mol. Catal.* **2018**, *455*, 108–120. [[CrossRef](#)]
37. Wu, P.; Jin, X.; Qiu, Y.; Ye, D. Recent progress of thermocatalytic and photo/thermocatalytic oxidation for VOCs purification over manganese-based oxide catalysts. *Environ. Sci. Technol.* **2021**, *55*, 4268–4286. [[CrossRef](#)]
38. Mulka, R.; Odoom-Wubah, T.; Tan, K.B.; Huang, J.; Li, Q. Biogenic Mn_xO_y as an efficient catalyst in the catalytic abatement of benzene: From kinetic to mathematical modeling. *Mol. Catal.* **2021**, *510*, 111643. [[CrossRef](#)]
39. Vorontsov, A. Selectivity of photocatalytic oxidation of gaseous ethanol over pure and modified TiO₂. *J. Catal.* **2004**, *221*, 102–109. [[CrossRef](#)]
40. Dai, Y.; Men, Y.; Wang, J.; Liu, S.; Li, S.; Li, Y.; Wang, K.; Li, Z. Tailoring the morphology and crystal facet of Mn₃O₄ for highly efficient catalytic combustion of ethanol. *Colloids Surf. A Physicochem. Eng. Asp.* **2021**, *627*, 127216. [[CrossRef](#)]
41. Li, J.-J.; Yu, E.-Q.; Cai, S.-C.; Chen, X.; Chen, J.; Jia, H.-P.; Xu, Y.-J. Noble metal free, CeO₂/LaMnO₃ hybrid achieving efficient photo-thermal catalytic decomposition of volatile organic compounds under IR light. *Appl. Catal. B Environ.* **2019**, *240*, 141–152. [[CrossRef](#)]
42. Morales, M.R.; Yeste, M.P.; Vidal, H.; Gatica, J.M.; Cadus, L.E. Insights on the combustion mechanism of ethanol and n-hexane in honeycomb monolithic type catalysts: Influence of the amount and nature of Mn-Cu mixed oxide. *Fuel* **2017**, *208*, 637–646. [[CrossRef](#)]
43. Chen, L.; Chen, P.; Wang, H.; Cui, W.; Sheng, J.; Li, J.; Zhang, Y.; Zhou, Y.; Dong, F. Surface lattice oxygen activation on Sr₂Sb₂O₇ enhances the photocatalytic mineralization of toluene: From reactant activation, intermediate conversion to product desorption. *ACS Appl. Mater. Interfaces* **2021**, *13*, 5153–5164. [[CrossRef](#)] [[PubMed](#)]

44. Parrino, F.; Palmisano, L. Reactions in the presence of irradiated semiconductors: Are they simply photocatalytic? *Mini-Rev. Org. Chem.* **2018**, *15*, 157–164. [[CrossRef](#)]
45. Azalim, S.; Franco, M.; Brahmi, R.; Giraudon, J.-M.; Lamonier, J.-F. Removal of oxygenated volatile organic compounds by catalytic oxidation over Zr–Ce–Mn catalysts. *J. Hazard. Mater.* **2011**, *188*, 422–427. [[CrossRef](#)]
46. Stobbe, E.R.; de Boer, B.A.; Geus, J.W. The reduction and oxidation behaviour of manganese oxides. *Catal. Today* **1999**, *47*, 161–167. [[CrossRef](#)]
47. Jabłońska, M. TPR study and catalytic performance of noble metals modified Al₂O₃, TiO₂ and ZrO₂ for low-temperature NH₃-SCO. *Catal. Commun.* **2015**, *70*, 66–71. [[CrossRef](#)]
48. Scirè, S.; Fiorenza, R.; Gulino, A.; Cristaldi, A.; Riccobene, P.M. Selective oxidation of CO in H₂-rich stream over ZSM5 zeolites supported Ru catalysts: An investigation on the role of the support and the Ru particle size. *Appl. Catal. A Gen.* **2016**, *520*, 82–91. [[CrossRef](#)]